

Deep learning method for enhancing luminescence image resolution

Priya Dwivedi, Juergen W. Weber, Robert Lee Chin, Thorsten Trupke, Ziv Hameiri *

University of New South Wales, Sydney, Australia



ABSTRACT

Luminescence imaging is a fast and non-destructive method to spatially resolve non-uniform electrical properties of solar cells. The spatial resolution of these images determines the smallest identifiable features. The higher the spatial resolution of an image, the better the capability to detect small defects. However, high-resolution cameras with high near-infrared light sensitivity that are suited to luminescence imaging of crystalline silicon are often expensive. In this study, we present a method, based on deep learning, that enhances the spatial resolution of luminescence images computationally with minimal cost. We also demonstrate the ability to overcome noise which is inevitable in any imaging system. This approach provides a simple and promising path toward reducing the cost of luminescence imaging systems and enhancing the capability of existing systems.

1. Introduction

Photovoltaics (PV) is arguably the most promising sustainable clean energy technology to satisfy the increasing energy demand of the world's growing population [1]. The extraordinary growth in PV in recent years is due to significant improvements in the performance of industrial silicon solar cells and simultaneous dramatic cost reduction [2]. Nonetheless, a further decrease in the cost is required to further accelerate the adoption of PV-generated electricity, and to meet the targets set by the Intergovernmental Panel on Climate Change (IPCC) [3]. One way to reduce the cost of solar cells and modules is by improving their reliability. This can be achieved by enhancing the capabilities of existing characterisation and process monitoring tools, ideally without increasing their cost.

Luminescence imaging is a key characterisation technique that provides spatially resolved information about the critical electrical parameters of solar cells [4,5]. It is widely used in PV research institutes and production lines [6]. According to the International Technology Roadmap for Photovoltaics (ITRPV) [7], electroluminescence (EL) systems will be integrated into >80% of solar cell production lines by 2029. High-resolution luminescence images are desirable as they enable more accurate and reliable identification of small defects and faults such as micro-cracks [8]. EL is also used to inspect large utility-scale PV plants [9]. To increase the throughput of these measurements, image acquisition with a large field of view (FOV) is preferred. However, for a given camera and lens, the resolution and FOV are inversely related. Increasing FOV reduces the detectable finer details of the subject. Hence, improving the resolution without reducing the FOV using a

computational approach will be very beneficial for outdoor inspection.

The straightforward approach to increasing image resolution is based on hardware modification, such as using a higher resolution sensor with a larger number of pixels [10]. Fitting a larger number of pixels onto a sensor may involve increasing the sensor size or decreasing the pixel size [11,12]. Increasing the sensor size is costly [10], since the sensor cost typically scales in proportion to its area. Decreasing the pixel size, on the other hand, reduces the amount of light received by each pixel resulting in an increase in the shot noise and ultimately requiring longer exposure time for the same signal-to-noise ratio (SNR) [11].

Single image super-resolution—a ubiquitous problem in computer vision—aims to extract a high-resolution image from a single low-resolution image [13]. Super-resolution (SR) algorithms have been used for a wide range of applications: satellite and aerial imaging [14], medical image processing [15], infrared imaging [16], hyperspectral imaging [17], facial images [18], and many more [19]. These algorithms can be broadly divided into two groups: image processing-based techniques [10] and deep neural network-based techniques [19]. Simple image processing approaches include the bicubic [20] and Lanczos [21] methods. The bicubic interpolation is often used as a baseline method for comparison [19,22–25]; it is based on a cubic interpolation on the nearest 4 × 4 pixels. More powerful image processing methods use image priors, and internal patch recurrence [26–28]. From the deep learning-based techniques, the SR convolutional neural network (SR-CNN) was the pioneer method to solve SR problems [23]. Shortly after, a fast super-resolution CNN (FSR-CNN) was proposed and demonstrated to be 40 times faster than SR-CNN [29]. As the deep learning research progressed, SR techniques based on neural networks

* Corresponding author.

E-mail address: z.hameiri@unsw.edu.au (Z. Hameiri).

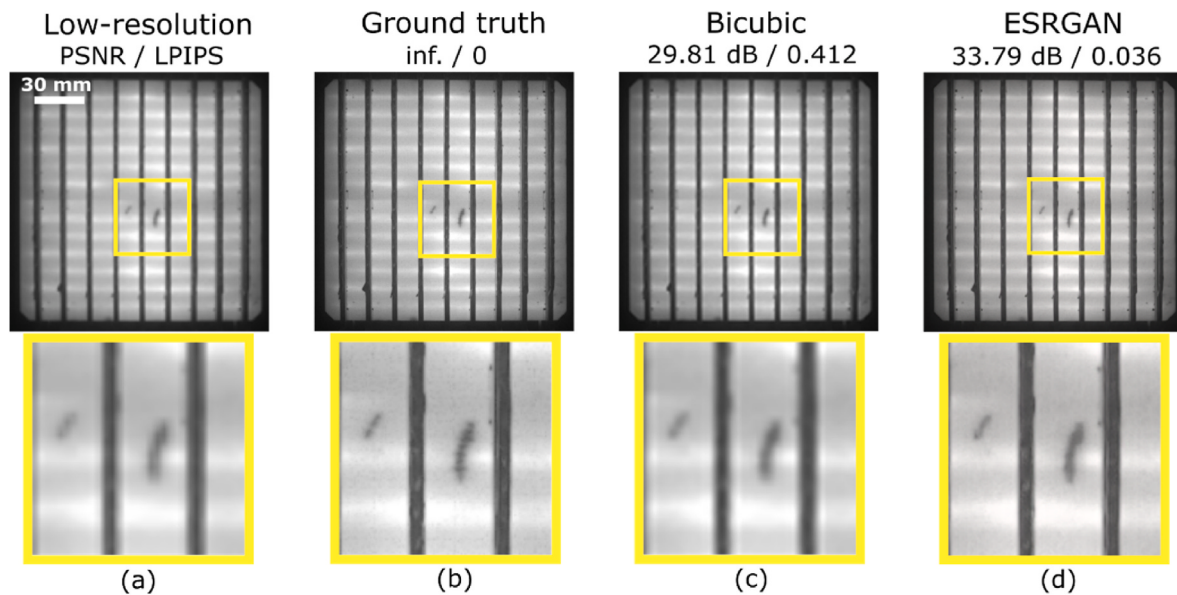


Fig. 1. A representative low-resolution image (130×130 pixels) from the test dataset (a), the corresponding ground truth [(b), (520×520 pixels)], and upsampled images by a factor 4×4 using bicubic (c) and ESRGAN (d). Pixel counts for all the images range [0, 255].

have been shown to extract even finer details and produce high-quality images [25,30–34]. Recently, generative adversarial networks (GAN)-based approaches were suggested for the SR problem [22,24,32]. From those, the enhanced super-resolution GAN (ESRGAN) [22] seems to be a promising approach. Instead of using a standard discriminator [35], it uses a relativistic discriminator [36]. Moreover, it uses improved perceptual loss and network structures which results in improved sharpness, and realistic texture details [22]. To date, ESRGAN has been used for applications in fluid dynamics, medical imaging, and remote sensing [37–41]. It has not been used for PV applications. In this study, we use ESRGAN to enhance the spatial resolution of luminescence images [42].

2. Methodology

2.1. Datasets

The efficacy of the developed deep learning network is demonstrated using EL and photoluminescence (PL) images of commercial mono-crystalline silicon solar cells. The training dataset contained 26,489 EL images with a resolution of 520×520 pixels, including 16,489 images of nine-busbar cells and 10,000 images of five-busbar cells. For robustness, 3,000 PL images with a resolution of 1860×1860 pixels of nine-busbars solar cells were also included in the dataset. The original EL and PL images were down sampled by a factor of 4×4 and 2×2 , respectively, using a bicubic interpolation [20]. The resultant images [130×130 pixels (EL) and 930×930 pixels (PL)] were used as the low-resolution images while the original images were used as the ‘high-resolution’ [‘ground truth’] images for the training. To make the network noise-resistant, a small amount of Gaussian noise with zero mean and a range of standard deviation from 0.001 to 0.1 was added to the low-resolution images with a probability of 0.5 during the training.

The test dataset, unseen by the network, contained 438 EL images and 881 PL images of nine-busbar cells and was used for assessing the performance of the trained algorithm. To evaluate the network performance in the presence of severe defects that were not contained in the training set, different shapes, including varying the width of lines, circles, triangles, zigzags, etc., were manually added to some of the EL images of the test dataset. To assess the impact of noise on the performance of the network, additional shot noise [43], resulting in SNR of 10, 33, and 105, was introduced to the low-resolution EL images of the test

dataset. Here, the SNR is defined as the ratio between the mean and the standard deviation of a pixel with the maximum count.

The network was experimentally validated using 881 paired high-resolution (1860×1860 pixels) and corresponding low-resolution (930×930 pixels) PL images of solar cells. In contrast to the test dataset consisting of pairs of original and down sampled images, the experimental validation was based on experimental data, including a high- and low-resolution image for each cell. Two PL imaging systems were used to collect this unique dataset. Each solar cell was imaged once by each system. For low-resolution images, a lens with 28 mm focal length and 360 mm FOV was used, while for HR images, a lens with 50 mm focal length and 180 mm FOV was employed. During the validation, 781 paired PL images were utilised to finetune the network while 100 paired PL images were used to test the network.

2.2. Network

As discussed, ESRGAN [22] was used in this study. A GAN consists of two types of networks: a generator and a discriminator [35]. The generator uses the low-resolution image as input data and creates a high-resolution trial image while the discriminator helps the generator by distinguishing the generated image from the real image. In our developed ESRGAN, the generator is a modified version of a super-resolution residual neural network (SRResNet) [32] and the discriminator is a relativistic discriminator [36] that is distinguished from the standard discriminator as follows: a standard discriminator estimates the probability of an input image as real or fake [35] while a relativistic discriminator estimates the probability that a given image is more realistic than a fake image [36]. For the optimisation of the model, three types of loss functions were used: perceptual [22], relativistic discriminator [36], and content loss [22].

We used an Intel® Xeon® W-2145 processor, with a central processing unit (CPU) clock speed of up to 3.70 GHz, an NVIDIA Titan V Graphical Processing Unit (GPU), and a random-access memory of 64 GB. The training time on this machine was approximately four hours. The time taken to generate high-resolution image depends on the spatial resolution of the low-resolution image. For example, enhancing an individual low-resolution image with a resolution of 130×130 pixels using the trained model is on the order of 100 ms.

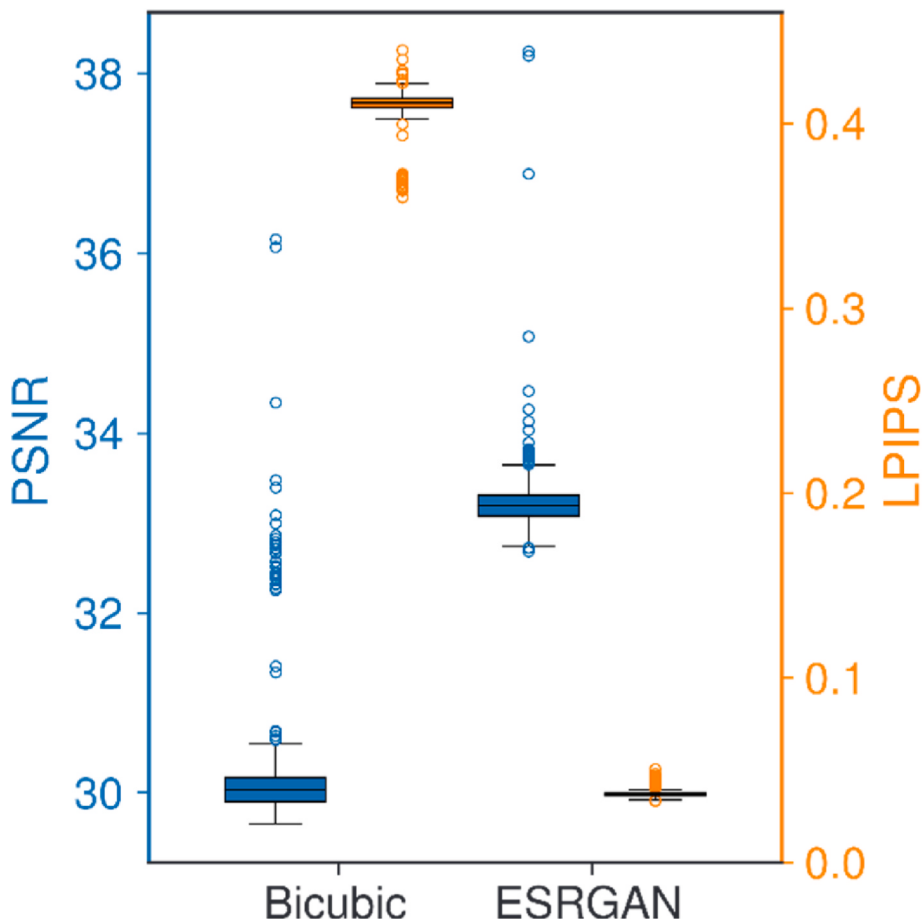


Fig. 2. PSNR (left axis) and LPIPS (right axis) distributions of the enhanced EL images of the test dataset. High PSNR and low LPIPS indicate better image matching.

2.3. Image quality assessment

2.3.1. Peak signal-to-noise ratio

Peak signal-to-noise ratio (PSNR) is one of the most popular image evaluation metrics for lossy transformations (i.e., image compression and image inpainting) [44]. If the ground truth and predicted images are denoted as I and \hat{I} , respectively, the PSNR is defined as:

$$\text{PSNR} = 10 \log_{10} \left(\frac{L^2}{\frac{1}{N} \sum_{i=1}^N [I(i) - \hat{I}(i)]^2} \right). \quad (1)$$

Here, $L = 255$ for an 8-bit image, and N is the number of pixels in the image. The PSNR depends on the pixel-wise loss between the predicted and ground truth images. It ranges from zero to infinity, where a PSNR of zero indicates that the reconstructed image is completely different from the ground truth image while a PSNR of infinity indicates that the reconstructed image is identical to the ground truth. As the PSNR is in logarithmic scale, a small variation in PSNR indicates a large variation in the pixel-wise loss. In this study, a PSNR above 32.0 dB is considered very good based on the visual inspection of multiple images.

The PSNR sometimes fails to capture the visual perception—two images with similar PSNRs may visually look different [44]. Therefore, in this study, an additional image metric is used to evaluate the results.

2.3.2. Learned perceptual image patch similarity

Learned perceptual image patch similarity (LPIPS) is the distance between a neural network's deep features of the ground truth and

generated images [45]. In Ref. [45], a neural network was trained for the classification task but was adapted for image similarity. One of the three networks was proposed to use: VGG [46], AlexNet [47], and SqueezeNet [48]. In our study, SqueezeNet was used due to its lightweight nature while still providing comparable accuracy [45]. The main advantage of this metric is its good agreement with human perception compared to other full reference metrics [49]. Identical images have an LPIPS of zero while higher values of LPIPS indicate a perceptual difference between the two images. In this study, an LPIPS below 0.05 is considered very good based on the inspection of multiple images.

3. Results

Fig. 1 presents representative EL images of a solar cell from the test dataset containing distinct defects. **Fig. 1(a)** shows the low-resolution image created computationally from the ground truth image, shown in **Fig. 1(b)**. The resolution is then computationally enhanced using the two techniques: a bicubic interpolation [**Fig. 1(c)**] and the developed ESRGAN [**Fig. 1(d)**]. To aid visual inspection, zoomed-in images of regions with distinct defects are presented below each image. It can be clearly seen that even the smallest features such as the pins along the busbar or a scratch mark are successfully reconstructed. The inserts also demonstrate that the ESRGAN-based method outperforms the bicubic interpolation, creating a significantly sharper image. To quantify the enhanced image quality, the PSNR and LPIPS are also provided. As discussed, if the generated image is identical to the ground truth image, the PSNR and LPIPS will be infinity and zero, respectively. For the presented representative solar cell, the ESRGAN-enhanced image has >13% higher PSNR and >90% lower LPIPS than the bicubic-enhanced image. Note that the PSNR values are on a logarithmic scale.

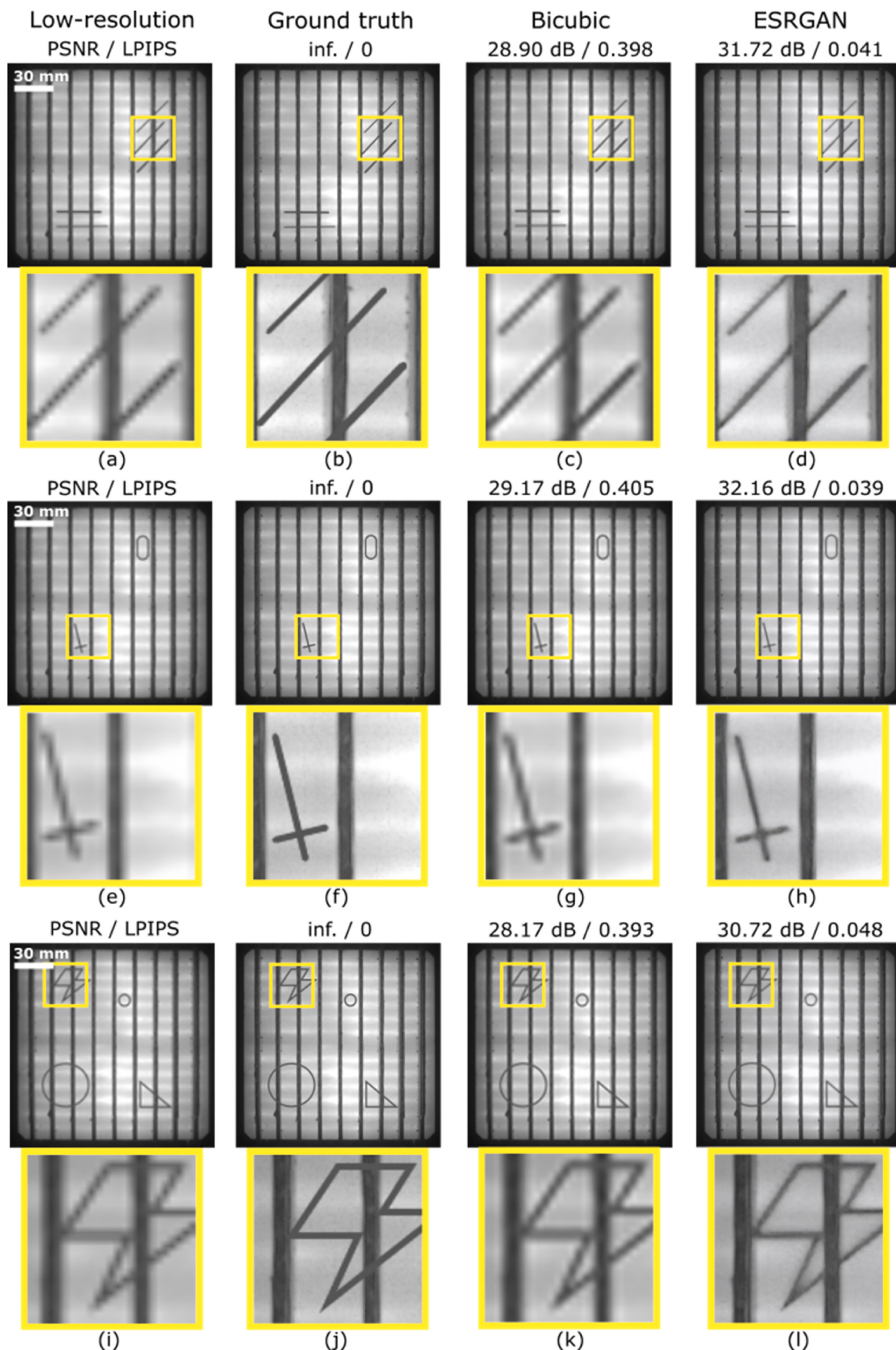


Fig. 3. Low-resolution images [(a,e,i)] with artificial, manually added marks that were not present in the training dataset, the corresponding ground truth images [(b,f,j)], and enhanced images using bicubic [(c,g,k)] and ESRGAN [(d,h,l)]. Pixel counts for all the images range [0, 255].

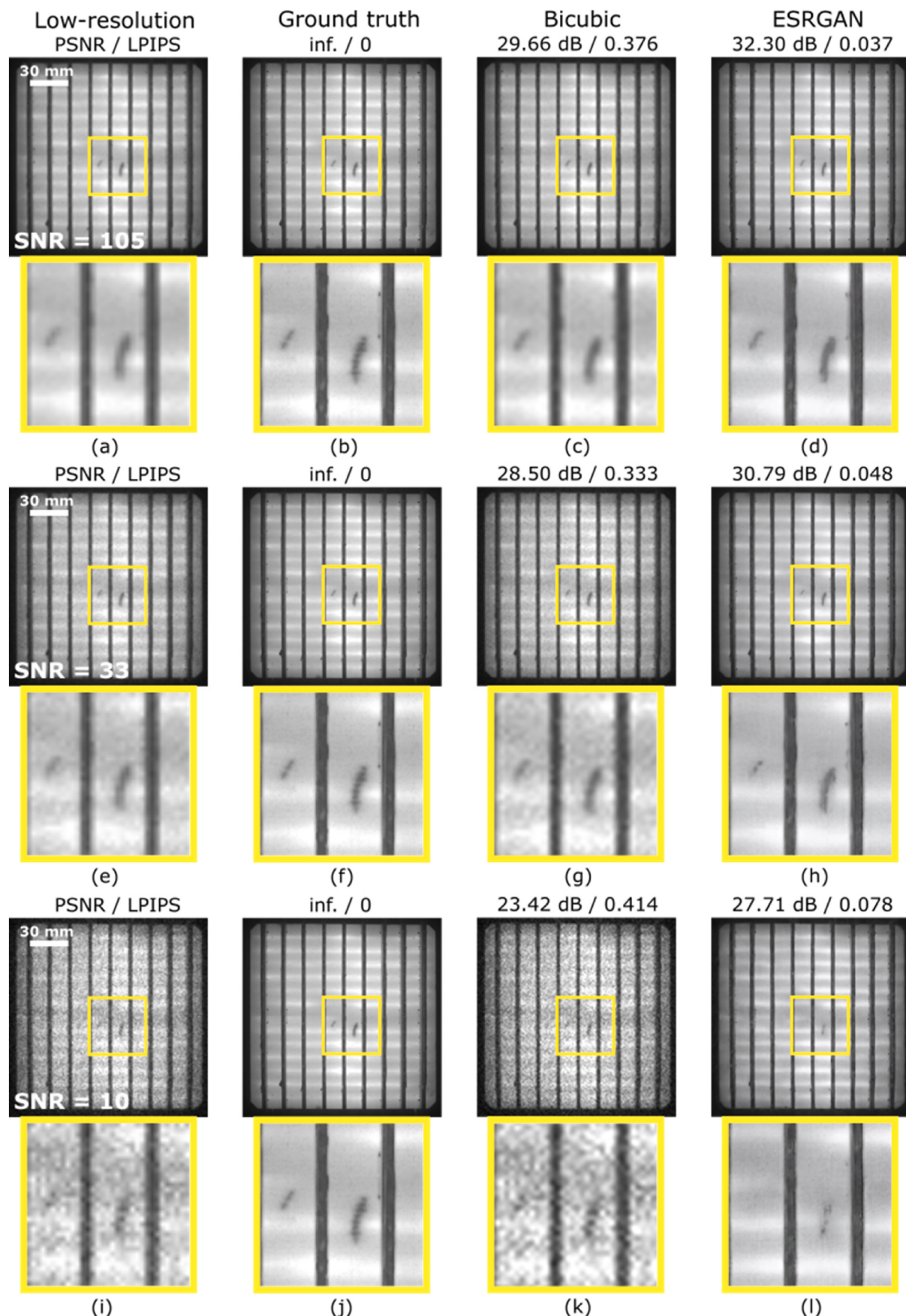


Fig. 4. Low-resolution images [(a,e,i)] with added noise with SNR of 105, 33, and 10; the corresponding ground truth images [(b,f,j)]; enhanced images using bicubic [(c,g,k)] and ESRGAN [(d,h,l)]. Pixel counts for all the images range [0, 255].

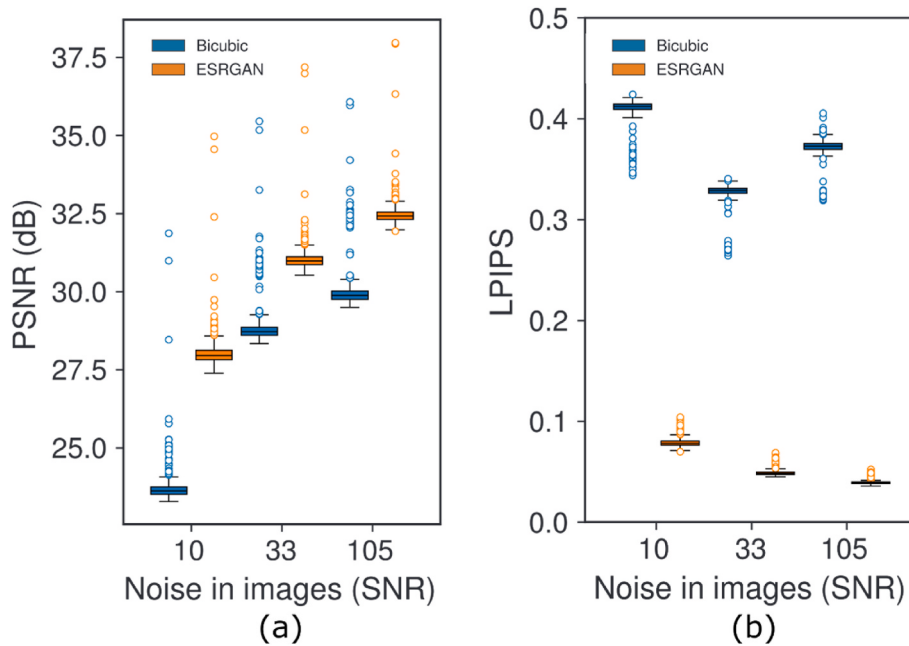


Fig. 5. Image metrics distributions for varying amounts of noise: PSNR (a), and LPIPS (b). High PSNR and low LPIPS indicate better image matching.

The distributions of PSNR and LPIPS values for the entire test dataset (438 images) are shown in Fig. 2 for the bicubic interpolation and ESRGAN. Images that were enhanced using ESRGAN have a 10.5% higher median PSNR and >91% lower median LPIPS than the bicubic-enhanced images. These trends demonstrate the superior performance of ESRGAN compared to the traditional bicubic-interpolation image processing technique.

As discussed, to investigate the performance of the developed network in extreme cases, EL images were generated with severely “defective” regions using a variety of shapes: lines with varying widths, crosses, circles, triangles, zigzags, etc. The marks were added manually to the *test* ground truth images; these images were then down sampled to create low-resolution images. The low-resolution images were used as input to the bicubic and ESRGAN interpolations to enhance their spatial resolution. Note that these artificial marks were *not* present in any images of the training dataset and therefore provide strong evidence for the network’s ability to up sample unknown image features. Fig. 3 presents representative low-resolution images [(a,e,i)], ground truth images [(b,f,j)], as well as corresponding enhanced images using the bicubic interpolation [(c,g,k)], and ESRGAN [(d,h,l)]. Results show that when using ESRGAN, all the marks are successfully up sampled and that the ESRGAN-generated images are of superior quality compared to those based on the bicubic interpolation method. We tested the network on additional 15 images with similar severely “defective” regions. The distributions of PSNR and LPIPS are given in the appendix (Fig. A1). The results indicate that, as shown for the natural defects above, ESRGAN achieves significantly higher PSNR (31.85 dB compared to 29.03 dB for the bicubic) and lower LPIPS (0.042 compared to 0.405 for the bicubic).

Since noise is unavoidable in any imaging system, the developed ESRGAN was tested in the presence of additional shot noise. EL images with an SNR of 100 are considered good quality images [50]; SNR of 33 corresponds to acceptable, but high noise, whereas SNR of 10 corresponds to unacceptable noise in EL images. Fig. 4 presents low-resolution images with added noise [(a,e,i)], the ground truth images [(b,f,j)], bicubic-enhanced [(c,g,k)], and ESRGAN-enhanced [(d,h,l)] images. For SNR of 105, the PSNR of the ESRGAN-generated image is only 4.4% lower compared to the case of no noise (Fig. 1). Moreover, ESRGAN performs much better than the bicubic technique. On investigating ESRGAN-enhanced images visually, scratch marks and pins along the busbars are successfully reconstructed. For SNR of 33, visual

Table 1

Image metrics comparison for ESRGAN with respect to bicubic for different amounts of noise.

Metrics	Method	No noise	SNR = 105	SNR = 33	SNR = 10
PSNR	ESRGAN	33.19 dB	32.42 dB	30.98 dB	27.96 dB
	Bicubic	30.03 dB	29.87 dB	28.72 dB	23.61 dB
	Difference (%)	+10.5%	+8.5%	+7.8%	+18.4%
LPIPS	ESRGAN	0.036	0.039	0.048	0.078
	Bicubic	0.411	0.372	0.328	0.412
	Difference (%)	-91.2%	-89.5%	-85.3%	-81.0%

inspection shows the successful resolution enhancement and denoising, except for one of the pins along the busbar and the smaller scratch mark. For SNR of 10, the visual comparison indicates that small features were not reconstructed (as they are not discernible in the noisy low-resolution images) while larger features were retained. For even higher noise, deep learning methods that are specifically designed for denoising applications are more suitable [51].

Fig. 5 presents the distributions of the PSNR (a) and LPIPS (b) for bicubic- and ESRGAN-enhanced images for the test dataset with varying amounts of introduced noise as a function of the SNR. Table 1 summarises the PSNR and LPIPS values and highlights the superior performance of ESRGAN over the traditional image processing technique in the presence of noise. For example, the PSNR data for images with an SNR of 33 from the ESRGAN approach exceed the PSNR of originals with an SNR of 105 using the bicubic interpolation approach. In relation to the LPIPS metric, even the ESRGAN results for the lowest SNR (SNR of 10) are far superior to the values from the bicubic interpolation approach even for an SNR of 105.

Figs. 6 and 7 present the experimental validation results. Fig. 6 shows a representative low-resolution image (a), the ground truth image (b), a bicubic-enhanced image (c), and an ESRGAN-enhanced image (d). Note that the variation in mean pixel intensity between the low-resolution and ground truth image is because each pixel in high-resolution camera receives fewer photons compared to the pixel in low-resolution camera. On investigating the enhanced images, the ESRGAN-enhanced images demonstrate higher PSNR and lower LPIPS compared to the bicubic-enhanced images. Interestingly, zoomed-in images indicate that the ESRGAN-enhanced images have sharper features even compared to

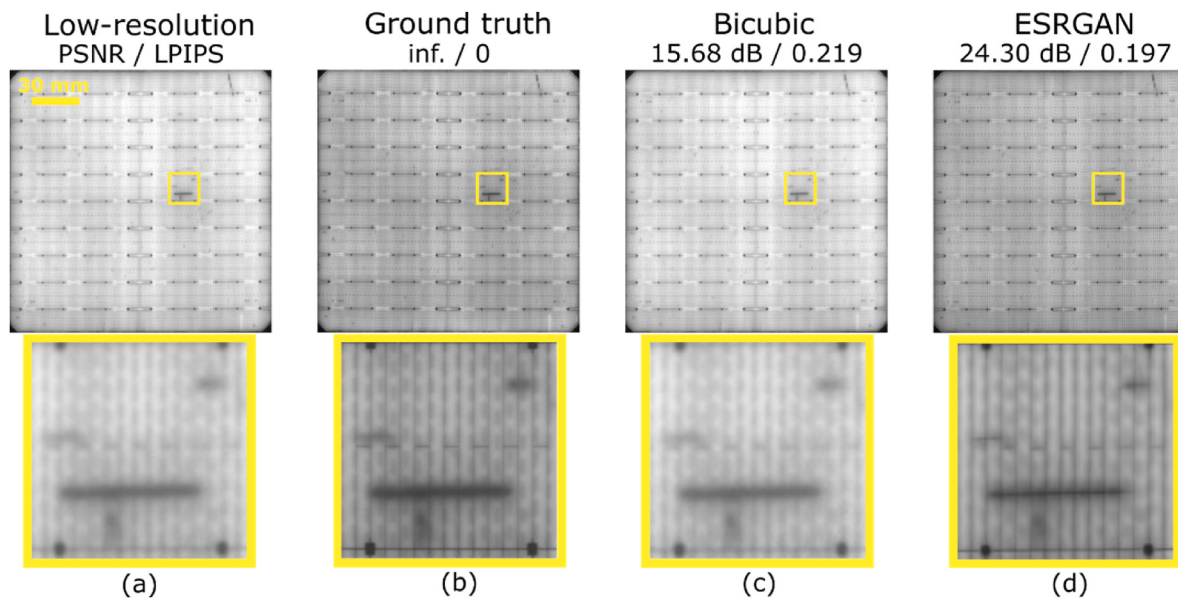


Fig. 6. A representative low-resolution image (a), the ground truth image (b), a bicubic-enhanced image (c), and an ESRGAN-enhanced image (d). Pixel counts for all the images range [0, 255].

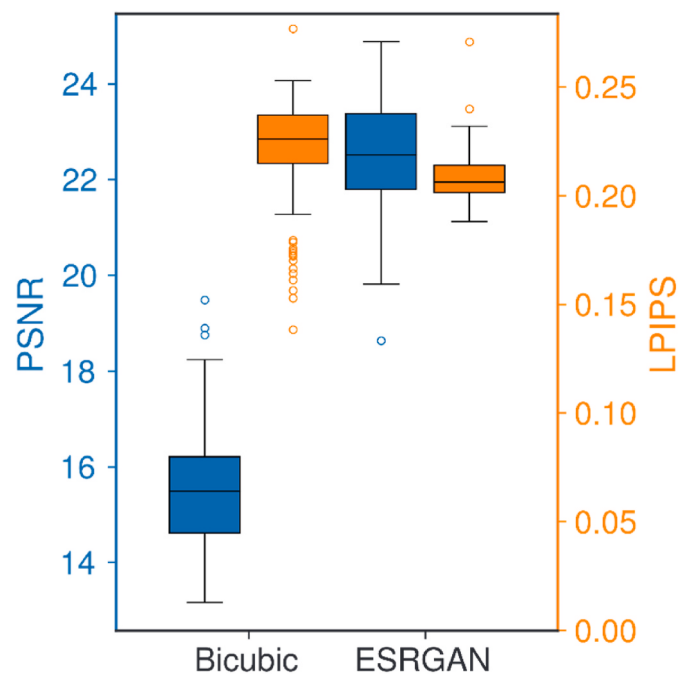


Fig. 7. PSNR and LPIPS distributions of the bicubic- and ESRGAN-enhanced images from the experimental validation. High PSNR and low LPIPS indicate better image matching.

the ground truth images. This suggests that the developed algorithm has successfully improved even the resolution of the ground truth images, which were initially captured by a real-world system with its own spatial resolution limitations (pixel size, noise, and point-spread function). Although the low-resolution image [Fig. 6(a)] has a higher mean pixel intensity compared to the ground truth image [Fig. 6(b)], the ESRGAN successfully reconstructed the original intensity variation whereas the bicubic could not. This is due to ESRGAN being a learning-based method that has learned these systematic variations, therefore, generates high-resolution images close to the ground-truth images.

Fig. 7 presents the distribution of the image metrics (PSNR and

LPIPS) for the test dataset (100 paired images). The ESRGAN-generated images have >45% higher median PSNR and ~9% lower median LPIPS compared to the bicubic unsampled images. It is interesting to notice that 14 bicubic-enhanced images have lower LPIPS than the ESRGAN-enhanced images. As mentioned in Section 2, one image metric may not be enough to capture the visual perception, therefore the results should be evaluated based on multiple image metrics and visual inspections. Detailed visual inspection (see Figs. A2 and A3 in the appendix) indicates that despite the higher LPIPS, the ESRGAN-enhanced images are better reconstructed and are closer to the ground truth images.

4. Conclusions

In this study, we present the use of a deep learning-based algorithm—ESRGAN—to enhance image spatial resolution of luminescence images taken on industrial silicon solar cells. We have shown that ESRGAN outperforms the traditional image processing algorithm, bicubic interpolation, for enhancing the spatial resolution of EL images. Markedly, new image features, which are not present in the training dataset, are also successfully enhanced. Furthermore, it has been shown that the developed network is highly resilient to image noise. The network can effectively eliminate noise while at the same time producing detailed images. Experimental validation using high- and low-resolution PL images taken on a set of solar cells, demonstrate that ESRGAN-enhanced images have higher PSNR and lower LPIPS than bicubic-enhanced images. Visual inspections indicate that the ESRGAN-enhanced images are almost indistinguishable from the ground truth images, and in some cases, are even better in terms of image sharpness. Our results for EL and PL images can be used as a steppingstone for enhancing the spatial resolution of other image modalities used in PV, such as infrared, ultraviolet fluorescence, hyperspectral, and optical images. We anticipate that these results can be employed in reducing the cost or enhancing the current performance of expensive imaging systems for the characterisation of solar cells and modules.

CRediT authorship contribution statement

Priya Dwivedi: Methodology, Investigation, Conceptualization, Writing - original draft, Writing - review & editing. Juergen W. Weber: Resources, Writing - review & editing. Robert Lee Chin: Resources,

Writing - review & editing. Thorsten Trupke: Methodology, Writing - review & editing. **Ziv Hameiri:** Supervision, Methodology, Funding acquisition, Conceptualization, Writing - original draft, Writing - review & editing.

Declaration of competing interest

The authors declare the following financial interests/personal relationships which may be considered as potential competing interests: Ziv Hameiri reports financial support was provided by Australian Renewable Energy Agency.

Data availability

Data will be made available on request.

Acknowledgement

This work was supported by the Australian Government through the Australian Renewable Energy Agency [ARENA; Project 2020/RND016]. The views expressed herein are not necessarily the views of the Australian Government, and the Australian Government does not accept responsibility for any information or advice contained herein.

Appendix A. Supplementary data

Supplementary data to this article can be found online at <https://doi.org/10.1016/j.solmat.2023.112357>.

References

- [1] F. Creutzig, P. Agoston, J.C. Goldschmidt, G. Luderer, G. Nemet, R.C. Pietzcker, The underestimated potential of solar energy to mitigate climate change, *Nat. Energy* 2 (9) (2017) 1–9.
- [2] M.A. Green, Commercial progress and challenges for photovoltaics, *Nat. Energy* 1 (1) (2016) 1–4.
- [3] D. Berney Needelman, J.R. Poindexter, R.C. Kurchin, I.M. Peters, G. Wilson, T. Buonassisi, Economically sustainable scaling of photovoltaics to meet climate targets, *Energy Environ. Sci.* 9 (6) (2016) 2122–2129.
- [4] T. Fuyuki, H. Kondo, T. Yamazaki, Y. Takahashi, Y. Uraoka, Photographic surveying of minority carrier diffusion length in polycrystalline silicon solar cells by electroluminescence, *Appl. Phys. Lett.* 86 (26) (2005), 262108.
- [5] T. Trupke, R.A. Bards, M.C. Schubert, W. Warta, Photoluminescence imaging of silicon wafers, *Appl. Phys. Lett.* 89 (4) (2006), 044107.
- [6] T. Trupke, B. Mitchell, J.W. Weber, W. McMillan, R.A. Bards, R. Kroeze, Photoluminescence imaging for photovoltaic applications, *Energy Proc.* 15 (2012) 135–146.
- [7] International Technology Roadmap for Photovoltaics (ITRPV), tenth ed., 2019.
- [8] M. Dhimish, V. Holmes, Solar cells micro crack detection technique using state-of-the-art electroluminescence imaging, *J. Sci.: Adv. Mat. Dev.* 4 (4) (2019) 499–508.
- [9] I. Høiaas, K. Gruijc, A.G. Imenes, I. Burud, E. Olsen, N. Belbachir, Inspection and condition monitoring of large-scale photovoltaic power plants: a review of imaging technologies, *Renew. Sustain. Energy Rev.* 161 (2022), 112353.
- [10] K. Nasrollahi, T.B. Moeslund, Super-resolution: a comprehensive survey, *Mach. Vis. Appl.* 25 (6) (2014) 1423–1468.
- [11] S.C. Park, M.K. Park, M.G. Kang, Super-resolution image reconstruction: a technical overview, *IEEE Signal Process. Mag.* 20 (3) (2003) 21–36.
- [12] V. Patanavijit, Super-resolution reconstruction and its future research direction, *AU. J. Techno* 12 (3) (2009) 149–163.
- [13] P. Milanfar (Ed.), Super-resolution Imaging, CRC Press, 2017.
- [14] Y. Wang, R. Fevig, R.R. Schultz, Super-resolution mosaicking of UAV surveillance video, in: 15th IEEE International Conference on Image Processing, 2008, pp. 345–348.
- [15] A. Gholipour, J.A. Estroff, S.K. Warfield, Robust super-resolution volume reconstruction from slice acquisitions: application to fetal brain MRI, *IEEE Trans. Med. Imag.* 29 (10) (2010) 1739–1758.
- [16] B. Narayanan, R.C. Hardie, K.E. Barner, M. Shao, A computationally efficient super-resolution algorithm for video processing using partition filters, *IEEE Trans. Circ. Syst. Video Technol.* 17 (5) (2007) 621–634.
- [17] H. Zhang, L. Zhang, H. Shen, A super-resolution reconstruction algorithm for hyperspectral images, *Signal Process.* 92 (9) (2012) 2082–2096.
- [18] Q. Yuan, L. Zhang, H. Shen, Multiframe super-resolution employing a spatially weighted total variation model, *IEEE Trans. Circ. Syst. Video Technol.* 22 (3) (2012) 379–392.
- [19] Z. Wang, J. Chen, S.C.H. Hoi, Deep learning for image super-resolution: a survey, *IEEE Trans. Pattern Anal. Mach. Intell.* 43 (10) (2021) 3365–3387.
- [20] R. Keys, Cubic convolution interpolation for digital image processing, *IEEE Trans. Acoust. Speech Signal Process.* 29 (6) (1981) 1153–1160.
- [21] C.E. Duchon, Lanczos filtering in one and two dimensions, *J. Appl. Meteorol. Climatol.* 18 (8) (1979) 1016–1022.
- [22] X. Wang, et al., ESRGAN: Enhanced Super-resolution Generative Adversarial Networks,” Presented at the European Conference on Computer Vision, ECCV, 2018.
- [23] C. Dong, C.C. Loy, K. He, X. Tang, Image super-resolution using deep convolutional networks, *IEEE Trans. Pattern Anal. Mach. Intell.* 38 (2) (2016) 295–307.
- [24] M.S.M. Sajjadi, B. Scholkopf, M. Hirsch, EnhanceNet: single image super-resolution through automated texture synthesis, *IEEE Int. Conf. Comput. Vis.* (2017) 4491–4500.
- [25] Y. Tai, J. Yang, X. Liu, C. Xu, MemNet: a persistent memory network for image restoration, in: IEEE International Conference on Computer Vision, ICCV, 2017, pp. 4549–4557.
- [26] D. Glasner, S. Bagor, M. Irani, Super-resolution from a single image, in: 12th IEEE International Conference on Computer Vision, 2009, pp. 349–356.
- [27] K.I. Kim, Y. Kwon, Single-image super-resolution using sparse regression and natural image prior, *IEEE Trans. Pattern Anal. Mach. Intell.* 32 (6) (2010) 1127–1133.
- [28] J. Sun, Z. Xu, H.-Y. Shum, Image super-resolution using gradient profile prior, in: IEEE Conference on Computer Vision and Pattern Recognition, 2008, pp. 1–8.
- [29] C. Dong, C.C. Loy, X. Tang, Accelerating the super-resolution convolutional neural network, in: European Conference on Computer Vision, ECCV, 2016, pp. 391–407.
- [30] J. Kim, J.K. Lee, K.M. Lee, Accurate image super-resolution using very deep convolutional networks, in: IEEE Conference on Computer Vision and Pattern Recognition, CVPR, 2016, pp. 1646–1654.
- [31] J. Kim, J.K. Lee, K.M. Lee, Deeply-recursive convolutional network for image super-resolution, in: IEEE Conference on Computer Vision and Pattern Recognition, CVPR, 2016, pp. 1637–1645.
- [32] C. Ledig, et al., Photo-realistic single image super-resolution using a generative adversarial network, in: IEEE Conference on Computer Vision and Pattern Recognition, CVPR, 2017, pp. 105–114.
- [33] Y. Tai, J. Yang, X. Liu, Image super-resolution via deep recursive residual network, in: IEEE Conference on Computer Vision and Pattern Recognition, CVPR, 2017, pp. 2790–2798.
- [34] Y. Zhang, Y. Tian, Y. Kong, B. Zhong, Y. Fu, Residual dense network for image super-resolution, in: IEEE Conference on Computer Vision and Pattern Recognition, CVPR, 2018, pp. 2472–2481.
- [35] I. Goodfellow, et al., Generative adversarial networks, *Commun. ACM* 63 (11) (2020) 139–144.
- [36] A. Jolicoeur-Martineau, The Relativistic Discriminator: a Key Element Missing from Standard GAN, 2018 [arXiv:1807.00734](https://arxiv.org/abs/1807.00734).
- [37] Z. Deng, C. He, Y. Liu, K.C. Kim, Super-resolution reconstruction of turbulent velocity fields using a generative adversarial network-based artificial intelligence framework, *Phys. Fluids* 31 (12) (2019), 125111.
- [38] L. Zha, Y. Shi, J. Wen, A lightweight image super-resolution network based on ESRGAN for rapid tomato leaf disease classification, in: The International Conference on Image, Vision and Intelligent Systems, ICIVIS, 2022, pp. 97–110, 2021.
- [39] Z. Hongtao, Y. Shinomiya, S. Yoshida, 3D brain MRI reconstruction based on 2D super-resolution technology, in: IEEE International Conference on Systems, Man, and Cybernetics, SMC, 2020, pp. 18–23.
- [40] T. Izumi, M. Amagasaki, K. Ishida, M. Kiyama, Super-resolution of sea surface temperature with convolutional neural network-and generative adversarial network-based methods, *J. Water. Clim. Change* 13 (4) (2022) 1673–1683.
- [41] J. Rabbi, N. Ray, M. Schubert, S. Chowdhury, D. Chao, Small-object detection in remote sensing images with end-to-end edge-enhanced GAN and object detector network, *Rem. Sens.* 12 (9) (2020) 1432.
- [42] P. Dwivedi, R. Lee Chin, T. Trupke, Z. Hameiri, A deep learning approach to increase luminescence image resolution of solar cells, in: 49th IEEE Photovoltaics Specialists Conference, 2022.
- [43] W. Schottky, Über spontane stromschwankungen in verschiedenen elektrizitätsleitern, *Ann. Phys.* 362 (23) (1918) 541–567.
- [44] Z. Wang, A.C. Bovik, Modern image quality assessment, *Synthesis Lectures on Image, Video, and Multimedia Processing* 2 (1) (2006) 1–156.
- [45] R. Zhang, P. Isola, A.A. Efros, E. Shechtman, O. Wang, The unreasonable effectiveness of deep features as a perceptual metric, in: IEEE/CVF Conference on Computer Vision and Pattern Recognition, 2018, pp. 586–595.
- [46] K. Simonyan, A. Zisserman, Very Deep Convolutional Networks for Large-Scale Image Recognition, 2015 [arXiv:1409.1556](https://arxiv.org/abs/1409.1556).
- [47] A. Krizhevsky, I. Sutskever, G.E. Hinton, ImageNet classification with deep convolutional neural networks, in: Advances in Neural Information Processing Systems, vol. 25, 2012.
- [48] F.N. Iandola, S. Han, M.W. Moskewicz, K. Ashraf, W.J. Dally, K. Keutzer, SqueezeNet: AlexNet-Level Accuracy with 50x Fewer Parameters And < 0.5 MB Model Size, 2016 [arXiv:1602.07360](https://arxiv.org/abs/1602.07360).
- [49] Y. Blau, R. Mechrez, R. Timofte, T. Michaeli, L. Zelnik-Manor, The 2018 PIRM challenge on perceptual image super-resolution, in: European Conference on Computer Vision, ECCV, 2018.
- [50] I. Zafirovska, Line Scan Photoluminescence and Electroluminescence Imaging of Silicon Solar Cells and Modules,” PhD Dissertation, The University of New South Wales, Sydney, Australia, 2019.
- [51] G. Liu, P. Dwivedi, T. Trupke, Z. Hameiri, A deep learning approach to denoise electroluminescence images of solar cells, in: 49th IEEE Photovoltaics Specialists Conference, 2022.